Available at https://www.iasj.net/iasj
Iraqi Academic Scientific Journals
Journal homepage:
https://journals.uokerbala.edu.iq/index.php/UOKJ

Research Article

Development and Validation of a 1-Year-Old Computational Voxel Phantom for Improved Dosimetric Accuracy in Paediatric Dental Cone Beam Computed Tomography

Nabeel Ibrahim Ashour

Department of Physics, College of Science, University of Kerbala, 56001 Karbala, Iraq.

Article Info Article history:
Received 24-11-2024
Received in revised form 9-12-2024
Accepted 15-12-2024
Available online 31 -12 - 2024
Keywords: Medical image data, 3DSlicer software, Monte Carlo, 3D voxel model, paediatric phantom design and effective dose.

Abstract

Cone Beam Computed Tomography (CBCT) offers a lower radiation dose alternative for paediatric patients compared to conventional CT scan, particularly in managing cleft lip and palate (CLP). Accurate dosimetry is essential to balance benefits and risks, with Monte Carlo simulations being a feasible approach. Despite advancements in computational phantoms, a gap exists for 1-year-old paediatric phantoms specific to CLP cases in dental CBCT. This study addresses this gap by developing and validating a 1-year-old voxel model for dental CBCT, utilising binary data from medical images as outlined in International Commission on Radiological Protection publication 143. The binary data were converted to voxel images using (X) MedCon software and processed in 3DSlicer to create a 3D model representing head and neck organs and tissues, including modifications for CLP anatomical variations. Validation against anthropometric data confirmed the model's accuracy. Monte Carlo GATE simulations were then used to calculate absorbed and effective organ doses during dental CBCT procedures. Effective dose (ED) values ranged from 0.02 mSv to 2.98 mSv, with dose reductions achieved by lowering the tube current-time product. The cochlea received the highest dose due to its proximity to the cone beam's field of view, while the brain and thyroid received the lowest doses due to protective anatomical positioning. The study provides a reliable dosimetry voxel phantom and emphasises optimising exposure parameters in paediatric imaging to minimise radiation risks.

Corresponding Author E-mail : nabeel.ashoor@uokerbala.edu.iq
Peer review under responsibility of Iraqi Academic Scientific Journal and University of Kerbala.

1 Introduction

Cone Beam Computed Tomography (CBCT) has emerged as a powerful imaging modality in dental applications, particularly in the diagnosis and management of craniofacial conditions such as Cleft Lip and Palate (CLP) in paediatric patients [1, 2]. CLP is a congenital deformity that requires precise imaging for effective treatment planning and follow-up. While conventional medical CT offers detailed imaging, its higher radiation dose, especially in paediatric patients, raises concerns due to the increased sensitivity of children to ionizing radiation[3, 4]. Radiation exposure in children is a critical issue, given their developing tissues and longer life expectancy, which heightens the risk of radiation-induced effects [5]. The biological effects of ionizing radiation can be broadly categorized into deterministic effects, which result from cell death and occur above a certain threshold, and stochastic effects, which include mutations that can lead to cancer and hereditary conditions. The risk of radiation-induced cancer has been extensively studied in various populations. Epidemiological data suggest that for the general population, a whole-body dose of 1,000 mSv increases the lifetime risk of fatal cancer by approximately 5%. However, in paediatric populations, this risk is significantly higher, with estimates indicating by a factor 2 or 3 increase in sensitivity compared to adults, even at lower doses typically encountered in medical imaging procedures [6].

CBCT, as a low-dose imaging alternative, presents a potential solution to reduce the radiation burden on paediatric patients, particularly in the context of CLP management [7]. However, accurate dosimetry is essential to ensure that the benefits of CBCT outweigh the risks. Overall, internal organ dosimetry can be performed by measurement with physical phantom containing dosimeters, or post-exam estimation with simulation software for the computational phantom [8]. Patients' direct internal measurements are considered infeasible. As a result, Monte Carlo methods demonstrate better feasibility for clinical dose assessment because they can accurately simulate the complicated radiation interactions and energy deposition in the human body [9]. Despite being very processor-intensive, the simulations may be expedited using graphics processing units (GPUs) [10]. The persistent increase in processing power indicates an imminent future in which Monte Carlo techniques may be routinely used for clinical dosimetry [11].

The development of computational voxel phantoms has been instrumental in improving dosimetric accuracy in medical imaging. These phantoms, which simulate the human body with detailed anatomical structures, are used in Monte Carlo simulations to calculate radiation doses to specific organs [12-14]. Despite the availability of several computational phantoms for adults [15-22], there is a notable gap in the literature concerning paediatric phantoms, particularly for 1-year-old children, which are critical for dosimetric studies in CBCT. The International Commission on Radiological Protection (ICRP) has developed reference paediatric computational phantoms, as documented in ICRP Publication 143 [23]. Which provides free medical image data without ethical approval, but these do not fully address the unique anatomical characteristics of children with CLP.

This study aims to address this gap by developing and validating a 1-year-old computational voxel phantom designed for dental CBCT use. The proposed phantom will be based on the reference paediatric computational phantom from ICRP 143 but will include modifications to account for the anatomical variations associated with CLP. The validation of the phantom will involve comparing morphometric parameters, such as head and neck dimensions, against the ICRP reference values. Following validation, Monte Carlo simulations will be employed to calculate organ and ED in the head and neck region, with particular attention to determining whether the dosimetric data for these organs exceed the average levels by a

factor of 2 or 3, as suggested by the literature. This study will not only contribute to

improving dosimetric accuracy in paediatric CBCT but also provide a valuable tool for clinicians in the management of CLP in young patients, ultimately enhancing the safety and efficacy of this essential imaging modality.

2 Methodology

2.1 Paediatric phantom construction

The method by which the paediatric (1-year-old) phantom was constructed is outlined in the following steps:

2.1.1 Tomographic data selection (Step 1)

The primary features of the paediatric reference phantom available in ICRP publication 143 were the fundamental factors used to construct our ICRP voxel model phantom [24], as displayed in Table 1. This reference document provides comprehensive information regarding various aspects, including voxel count, resolution, and total matrix size, for both the paediatric reference phantoms and their corresponding adult counterparts as outlined in publication 110 [25]. The study focused on a 1-year-old male model, with phantom data sourced from the updated directory on the ICRP 143 website [26]. This directory contains subfolders that contain critical data for the creation of computational models for paediatric phantoms, including ASCII, binary, blood, media, organs, and skeletons. The data consists of model information for different age groups and genders.

Table 1. Primary characteristics of the reference 1-year-old computational phantoms. Reproduced from ICRP143 [23].

Property	1-Year male
Thickness of Slice (voxel height, mm)	1.4
Resolution of Voxel in-plane (mm)	0.663
Voxel volume (mm^3)	0.615
Column number	393
Row number	248
Slice number	546

2.1.2 Binary data convert to voxel images (Step 2)

The binary data for 1- year- old male was chosen and the data sets of Table 1 were imported into the (X) MedCon software version (0.21.2) [27]. This software's graphical user interface (GUI) provides a visual interface for managing specific options to generate 2D medical image files (see Figure 1). The (X) MedCon facilities produced medical images that were preserved, and the file that resulted was labelled "binary.hdr."

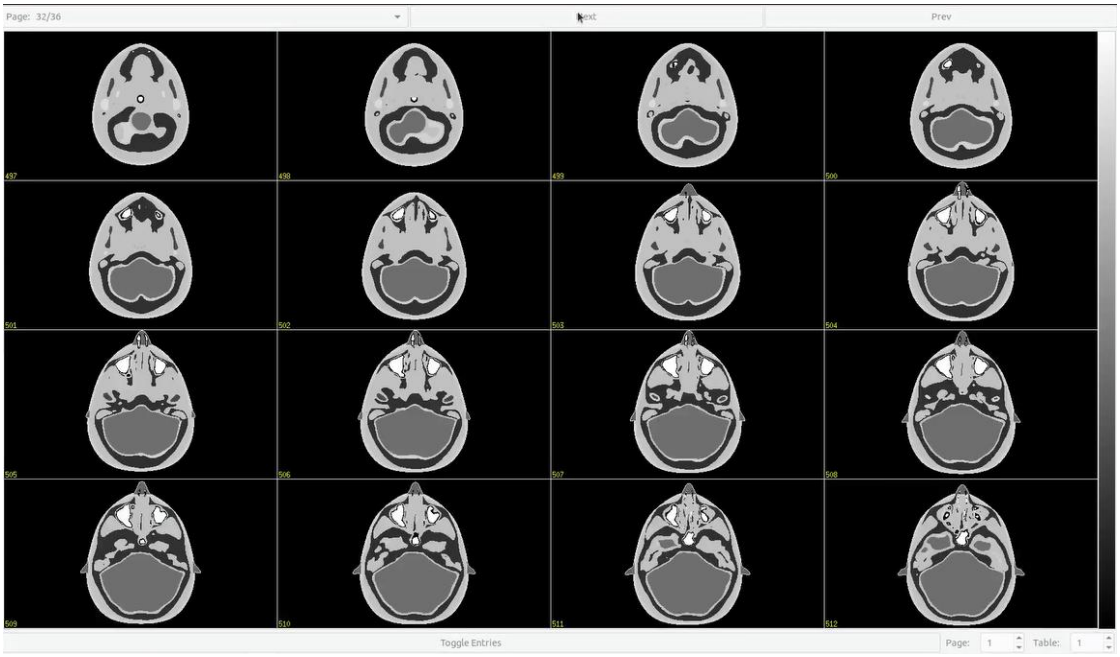

Figure 1. 2D medical image produced by converting binary image data utilising (X) MedCon.

2.1.3 Construction of paediatric voxel phantom (Step 3)

In this step, the 2D medical images that were saved as 'binary.hdr' were uploaded into 3DSlicer software, an open-access toolkit that assists in processing 2D, 3D, and 4D image data, encompassing, segmentation, surfaces, annotations, modifications, and additional functionalities [28]. Subsequently, Step 3 involves, several processing steps in 3DSlicer software, the voxel array stores a numerical value that aligns with the respective positions of the organ or tissue to represent the identification number (ID) of the organ. Consequently, a 3D model file was obtained representing a 1-year-old ICRP voxel phantom containing 1–140 organ/tissue regions [26].

The processing steps of the medical images in 3DSlicer software are termed voxelisation, as explained in Figure 2. In Figure 2(a), the 'Volumes' command of the modules was selected, and subsequently, from Table 1, the image spacing field values were selected to represent the resolution of the voxel in-plane (mm) and the thickness of the slice (voxel height, mm) (see Figure 2(b)). Figure 2(c) illustrates the visual representation of the ICRP voxel phantom for a 1-year-old male.

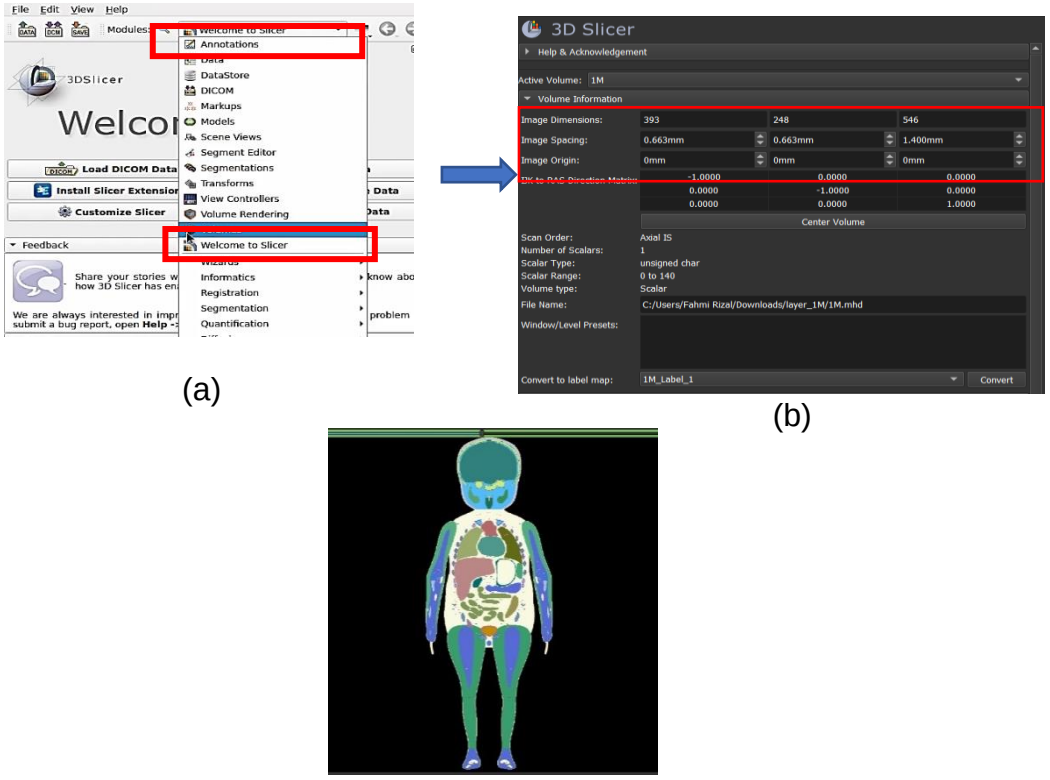

Figure 2. Transformation Process of La p Model: (a) Active Volume Selection, (b) Image Input Dimension and Spacing Details, and (c) Label Map Conversion represent ICRP voxel phantom.

2.1.4 Phantom validation (Step 4)

Once a 3D model phantom was obtained representing 1–140 organs and tissues of a 1-year-old ICRP voxel phantom. In this stage, anthropometric data from many literature sources were matched to the dimensions of the 3D model phantom. Three standard anthropometric measurements were taken: arm length, standing height, and head circumference. Reference heights for standing height alone are given in Publication 89 (ICRP, 2002) [29]. The National Health and Nutrition Examination Survey (NHANES) III (1988–1994) data set was employed to get 1-year-old head circumferences [30]. In addition, the 1-year-old phantoms' arm length and head circumference were obtained using the NHANES IV (1999-2002) survey [31]. The male and female phantoms were subjected to identical criteria at every age below fifteen years.

2.1.5 Methodology for cleft geometry (Step 5)

The methodology utilized in this study implicated the employment of ICRP voxel phantoms, accurately designed layer by layer to facilitate create the clefts. The 3D Slicer module's ruler tool was employed as a guide in the creation of these layers, which were generated using the Segmentation module to encompass the entire area of interest (see Figure 3(a)). A total of 18 layers were created from the top of the head to the base of the skull, with portions of the cervical spine and neck included, each with a uniform thickness of 1 cm. The initial segmentation set was completed without any modifications, thus preserving the original anatomical features.

Following this, layers 13 and 14 were specifically identified due to their anatomical relevance in covering the mouth and nose regions (see Figure 3(b)). The cleft geometry was modelled and edited to replicate specific anatomical conditions, which were integral to the study's focus on craniofacial structures, refer to Figure 3(c) [32-34]. After the cleft geometry was introduced and refined, all layers, including both the original, unaltered layers and the newly edited cleft layers, were combined, and converted into a comprehensive 3D model. This step ensured that the final model accurately reflected both the normal and modified anatomical features. For dosimetric simulation purposes, this 3D model was saved in '1M.mhd' format. The '1M.mhd' file can be uploaded to Monte Carlo GATE (Geant4 Application for Tomographic Emission).

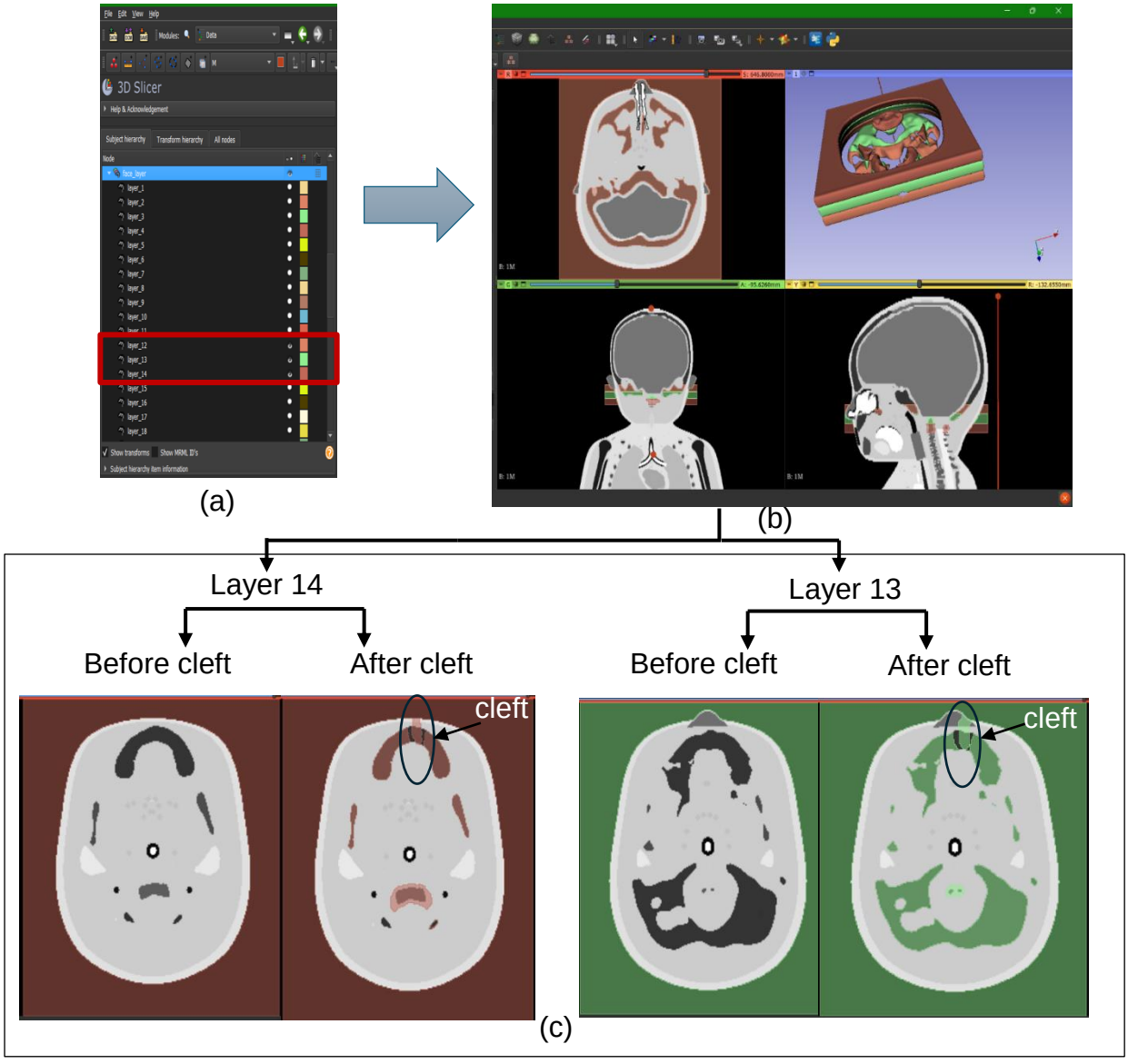

Figure 3. The process of cleft geometry using 3DSlicer.

2.2 Mont Carlo GATE simulation

To apply GATE simulation and calculate the ED of the chosen organs in the head and neck for our developed voxel phantom for the simulation of paediatric exams, the Planmeca Promax 3D classic system parameters were applied, which were simulated using the GATE code, after generating X-ray beams

using the Spekpy v2.0 software toolkit to create the cone shape of the X-rays in this simulation [35]. Since the acquisition parameters have shown significant impact on each of image quality and recorded doses [36], several exposure parameters provided by CBCT were also relied upon to calculate the ED to the organs. In order to simulate a standard CBCT scan for paediatrics' jaws, the beam parameters were selected, as shown in Table 2.

Table 2. Exposure parameters and indications of acquisition protocol.

Protocol resolution mode	Position	Tube voltage (kVp)	Tube loading (mAs)
High	Both jaws full rotation (360°)	90	110.8
Normal			38.3
Low			36.9
Low			19
Low			7.1

One of the tasks of this study was to achieve the same level of target coverage as that utilised in the diagnostic planning of CLP patients through GATE simulation. During GATE simulation, phase space is employed to gather the data of X-ray photons obtained from the diagnostic of the CLP. The field of view (FOV) is utilised to reduce the beam to the minimum size required for scanning the desired region. It is worth noting that the shortest FOV results in the lowest effective doses [16, 37]. Therefore, FOV was set to 68×68 mm^2, which is recommended for paediatric patients. During the simulation, the variable histories were modified according to each exposure parameter. The history is contingent upon the detector area (cm^2), fluence (photon/cm^2), milliampere-seconds product (mAs), and tube voltage (kVp). "DoseByRegions.txt" is a text file that records the absorbed doses (D) in mGy in organs following the GATE simulation. This file contains data on the distribution of radiation dosage in different areas of the patient's cranium and neck.

The equivalent dose (H_t) has been calculated for each tissue or organ by multiplying the absorbed dose (D) by the radiation weighting factor $\mathbb{W}_R$ (which is 1 for X-rays). Since $\mathbb{W}_R$ =1, the equivalent dose is numerically equal to the absorbed dose. Additionally, the ED in mSv was measured by sum the products of the equivalent dose (H_t) and the tissue weighting factors ω_t for all relevant sensitive organs that we selected for paediatric patients in this study [38]:

$$ED = \sum_t (H_t \times \omega_t) \dots\dots\dots\dots\dots\dots\dots\dots (1)$$

3 Results

In this study, all the results related to the validation of our ICRP voxel phantom (1-year-old) and additionally the dosimetric data during simulating dental CBCT by GATE are presented in this section.

3.1 Phantom validation analysis

Table 3 presents a comparison between the dimensions of the ICRP voxel phantom (1-year-old) and reference data from ICRP 143, focusing on key anthropometric parameters: head circumference, standing height, and arm length. The ICRP voxel phantom dimensions were measured using the 3DSlicer toolkit.

Table 3. Comparison of reference and ICRP voxel phantom values (mm) for morphometric parameters regarding some parts of the body.

Phantom	Head circumference			Standing height			Arm length		
	Ref	ICRP Phantom	%Diff	Ref	ICRP Phantom	%Diff	Ref	ICRP Phantom	%Diff
1-year-old M	47.3	47.3	0.0	76	76	0.0	32.6	32.6	0.0

M, male; %Diff, percentage difference.

3.2 Organ doses analysis by GATE simulation

The study employed a simulation approach where each exposure parameter was selected according to variable histories. Table 4 shows the dosimetric data, including the doses received by the organs and the exposure parameters (tube current-time product or mAs, and tube potential or kVp). The absorbed doses increased with the exposure parameters for the phantom organs. ED levels ranged from 0.02 mSv to 2.98 mSv, depending on the exposure settings. Lower exposure parameters led to decreased energy deposition in organs. For a 1-year-old phantom, ED reductions were noted when the tube current-time product was reduced from 110.5 mAs to lower values.

Table 4. The absorbed and effective doses for different exposure settings in the head and neck organs of a 1-year-old ICRP voxel phantom.

1-year-old	Absorbed Dose (mGy) by GATE simulation													ED (mSv)
Protocol mode	**Thyroid**	**Optic nerve**	**Optic chiasm**	**Left parotid**	**Right parotid**	**Left lens**	**Right lens**	**Left eye**	**Right eye**	**Left cochlea**	**Right cochlea**	**Brainstem**	**Brain**	
Low resolution 90 kVp ,7.1 mAs	0.01	0.01	0.01	0.02	0.02	0.006	0.005	0.01	0.01	0.024	0.022	0.03	0.01	0.02
Low resolution 90 kVp ,19 mAs	0.12	0.1	0.11	0.19	0.2	0.12	0.12	0.2	0.28	0.42	0.32	0.28	0.07	0.29
Low resolution 90 kVp ,36.9 mAs	0.2	0.25	0.26	0.39	0.42	0.3	0.33	0.36	0.37	0.75	0.7	0.5	0.12	0.57
Normal resolution 90 kVp ,38.3 mAs	0.22	0.57	0.55	0.6	0.66	0.5	0.53	0.45	0.4	1.03	1.11	0.95	0.15	0.90
High resolution 90 kVp ,110.5 mAs	0.65	1.95	2	2.72	2.7	1.75	1.81	1.23	1.3	3.46	3.24	2.1	0.4	2.98

Regarding Figure 4, which represents the following observations were recorded for the phantom at 1 year of age about the mean contribution of organ dosage to the total ED.

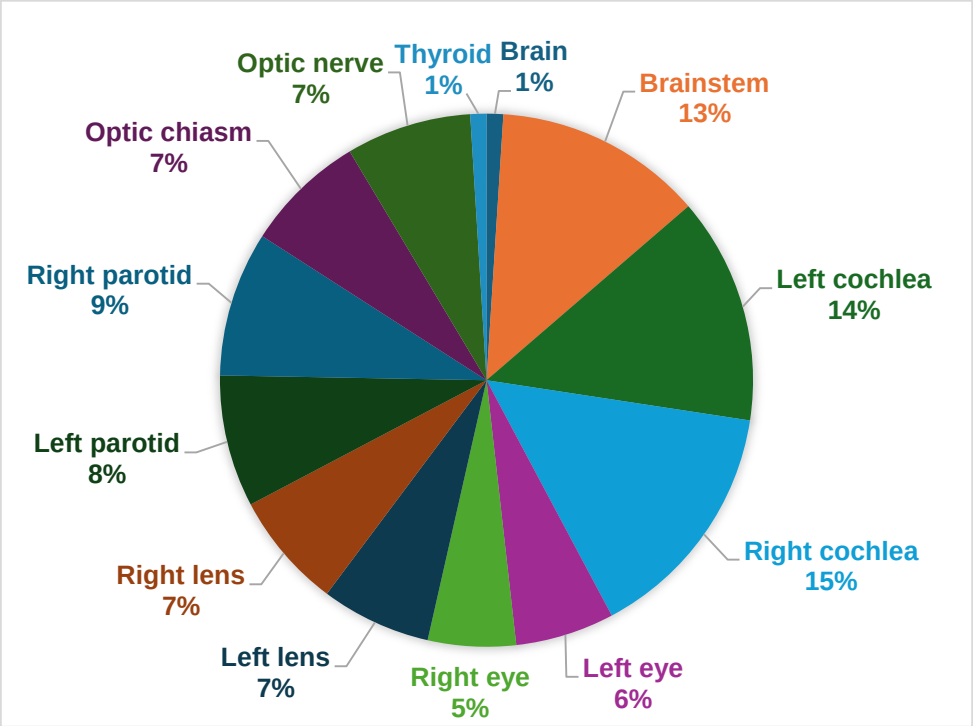

Figure 4. Proportional contribution of organ doses to the total ED for a 1-year-old ICRP voxel phantom using the CBCT protocol (38.325 mAs, 90 kVp) simulated by GATE.

4 Discussion

The study showed in Table 3 that the ratios depicting the disparity between the dimensions of the ICRP voxel phantom and the standard anthropometric data remained consistent across all measurements.

The patient's age significantly influences the magnitude of radiation risk, with paediatric patients being particularly susceptible. The study found that the cochlea absorbed the highest radiation doses due to their proximity to the cone beam's field of view. The brain and thyroid received the lowest doses, benefiting from protective anatomical positioning. The findings underscore the importance of optimising exposure parameters to minimise radiation risks in paediatric imaging. Although the risk of neoplasia in adults exposed to doses below 50 mSv has not significantly increased, the associated risk for younger patients is estimated to be 2-3 times higher [39]. Table 4 presents the ED values (in mSv) that fall within this acceptable range for paediatric patients. This highlights the necessity of stringent radiation protection measures for paediatric patients, especially in dental CBCT procedures.

One of the benefits of analysing the data in Figure 4 was to clarify which organ received the highest contribution of the dose in the field of view specified in this study. The exposure parameter (38.3 mAs, 90 kVp) showed that the right and left cochlea made the most significant contributions, at 15% and 14% of the total ED, respectively. The left and right cochlea had the largest average radiation dose contributions in the simulation because they are located within the cone beam's FOV (68 x 68) mm^2. Additionally, the brain and thyroid have the lowest contributions at 1% at the same exposure parameter. The brain

demonstrates low radiation dose absorption (1%) as a result of its location inside the skull bones, which effectively shields and absorbs the majority of the radiation doses. Whereas, the thyroid, due to its position out FOV (68 x 68) mm^2.

5 Limitations and future applications

The phantom described in this study is the computational model representing the 1–year–old male. This model was based on the main characteristics of paediatric reference computational phantoms and binary data of voxel images outlined in ICRP 143 [24], providing accurate digital 3D representations of human anatomy. It is important to note that although this phantom possesses organ/tissue masses corresponding to reference values from ICRP 143, it maintains the unique structure of each organ, including its contours, depth, and location, as seen in the reference data used to create it. Therefore, this model is unable to evaluate the amount of radiation absorbed by organs in individuals with varying body sizes and organ shapes. Although the main purpose of creating this computational phantom was to derive radiological protection values, it is acknowledged that it may be used for other purposes as well. However, it is crucial to remain aware of the specific limitations related to their intended use.

For future applications, the resulting 3D model can be exported in STL (stereolithography) format, the standard format used for 3D printing. This format can be chosen due to its compatibility with a wide range of 3D printers, enabling the precise reproduction of the model for further experimental use. The STL file can then be prepared and optimised for 3D printing, ensuring that the final printed model will accurately reflect the detailed anatomical and modified features as designed.

This study's significance lies in its determination of organ dosimetry. Furthermore, the existing phantom can also be used using non-standard exposure parameters from the CBCT that are less than (~90 kVp). This will create a full database of radiation doses and test the quality of diagnostic images. This underscores the need to achieve a judicious equilibrium between minimising radiation exposure and enhancing the quality of the image.

6 Conclusion

This study adopts a new method for developing and validating a 1-year-old computational voxel phantom designed for dental CBCT use. The phantom was based on the reference paediatric computational phantom from ICRP 143 but included modifications to account for the anatomical variations associated with CLP. The research offers valuable insights into the precision and dependability of the ICRP voxel phantom and the corresponding measurements of selected organs at risk dosage using GATE simulations for a 1-year-old individual. CBCT protocols have been simulated as a diagnostic technique for dosimetry. The anthropometric measurements of the ICRP voxel phantom, including head circumference, standing height, and arm length, were in line with established reference data, confirming its dependability for dosimetric simulations.

The dosimetric results demonstrated a clear relationship between increased exposure parameters (tube potential and tube current-time product) and absorbed organ doses. The ED values ranged from 0.02 mSv to 2.98 mSv. The ED was dramatically reduced by decreasing the tube current-time product (mAs), demonstrating the possibility of optimising the dose in paediatric imaging techniques using CBCT. The research highlighted the need to tightly control radiation exposure in paediatric imaging by identifying ED levels within the permissible risk range for paediatric patients. Due to their locations within the field of view, the right and left cochlea organs had the largest dose contributions, but the thyroid gland and brain showed the lowest contributions, due to the protective position of the brain within the skull absorbing most of the radiation, while the position of the thyroid gland is outside the field of view. In conclusion, the study underscores the necessity for tailored

dosimetric approaches in paediatric imaging to mitigate radiation risks, with the validated ICRP voxel phantom and detailed dose analysis through GATE simulations providing a robust framework for optimising exposure parameters and enhancing the safety and effectiveness of radiological practices for young patients.

Acknowledgment

I would like to thank the researchers and authors at Department of Physics, Collage of Science, University of Kerbala and Department of Biomedical Imaging, Faculty of Medicine, Universiti Malaya for their insightful efforts and discussion of the manuscript which contributed to making this research study readable.

Declaration of competing interest

The author reported no potential conflicts of interest.

Funding

The study was conducted without financial support

Ethical approval

Not required

7 References

1. Shrestha, A., M. Takahashi, T. Yamaguchi, M. Adel, M. Furuhata, Y. Hikita, H. Yoshida, T. Nakawaki, and K. Maki, *Three-dimensional evaluation of mandibular volume in patients with cleft lip and palate during the deciduous dentition period.* Angle Orthod, 2020. **90**(1): p. 85-91.
2. Bromberg, N. and M. Brizuela, *Dental cone beam computed tomography.* 2023.
3. Frush, D.P., L.F. Donnelly, and N.S. Rosen, *Computed tomography and radiation risks: what pediatric health care providers should know.* Pediatrics, 2003. **112**(4): p. 951-957.
4. Gustavo M. Santaella, D., MS, PhD, Bruno C. Azevedo, DDS, MS and William C. Scarfe, BDS, FRACDS, MS, *Imaging Techniques for Patients with Cleft Lip and/or Palate.* The journal of professional excellence dimensions of dental hygiene, 2022.
5. Haridasan, P., *Unscear 2013 Report.* Radiation Protection and Environment, 2013. **36**(3): p. 143-143.
6. Valentin, J., *Radiation and your patient: A guide for medical practitioners:ICRP Supporting Guidance 2: Approved by ICRP Committee 3 in September 2001.* Annals of the ICRP, 2001. **31**(4): p. 1-52.
7. Han, M., H.J. Kim, J.W. Choi, D.Y. Park, and J.G. Han, *Diagnostic usefulness of cone-beam computed tomography versus multi-detector computed tomography for sinonasal structure evaluation.* Laryngoscope Investig Otolaryngol, 2022. **7**(3): p. 662-670.
8. Pernicka, F. and I. McLean, *Dosimetry in diagnostic radiology: an international code of practice*. 2007: International Atomic Energy Agency Vienna, Austria.
9. Fum, W.K., J.H.D. Wong, and L.K. Tan, *Monte Carlo-based patient internal dosimetry in fluoroscopy-guided interventional procedures: A review.* Physica Medica, 2021. **84**: p. 228-240.
10. Badal, A., F. Zafar, H. Dong, and A. Badano. *A real-time radiation dose monitoring system for patients and staff during interventional fluoroscopy using a GPU-accelerated Monte Carlo simulator and an automatic 3D localization system based on a depth camera*. in *Medical Imaging 2013: Physics of Medical Imaging*. 2013. SPIE.
11. Roser, P., X. Zhong, A. Birkhold, N. Strobel, M. Kowarschik, R. Fahrig, and A. Maier, *Physics-driven learning of x-ray skin dose distribution in interventional procedures.* Medical Physics, 2019. **46**(10): p. 4654-4665.
12. Borbinha, J., S. Di Maria, P. Madeira, A. Belchior, M. Baptista, and P. Vaz, *Increasing organ dose accuracy through voxel phantom organ matching with individual patient anatomy.* Radiation Physics and Chemistry, 2019. **159**: p. 35-46.
13. Griffin, K., C. Paulbeck, W. Bolch, H. Cullings, S. Egbert, S. Funamoto, T. Sato,

A. Endo, N. Hertel, and C. Lee, *Dosimetric Impact of a New Computational Voxel Phantom Series for the Japanese Atomic Bomb Survivors: Children and Adults.* Radiat Res, 2019. **191**(4): p. 369-379.
14. Hunt, J.G., F.C. da Silva, C.L. Mauricio, and D.S. dos Santos, *The validation of organ dose calculations using voxel phantoms and Monte Carlo methods applied to point and water immersion sources.* Radiat Prot Dosimetry, 2004. **108**(1): p. 85-9.
15. Vassileva, J. and D. Stoyanov, *Quality control and patient dosimetry in dental cone beam CT.* Radiation protection dosimetry, 2010. **139**(1-3): p. 310-312.
16. Pauwels, R., J. Beinsberger, B. Collaert, C. Theodorakou, J. Rogers, A. Walker, L. Cockmartin, H. Bosmans, R. Jacobs, and R. Bogaerts, *Effective dose range for dental cone beam computed tomography scanners.* European journal of radiology, 2012. **81**(2): p. 267-271.
17. Morant, J., M. Salvadó, I. Hernández-Girón, R. Casanovas, R. Ortega, and A. Calzado, *Dosimetry of a cone beam CT device for oral and maxillofacial radiology using Monte Carlo techniques and ICRP adult reference computational phantoms.* Dentomaxillofacial Radiology, 2013. **42**(3): p. 92555893.
18. Kim, D.-S., O. Rashsuren, and E.-K. Kim, *Conversion coefficients for the estimation of effective dose in cone-beam CT.* Imaging science in dentistry, 2014. **44**(1): p. 21-29.
19. Ludlow, J., R. Timothy, C. Walker, R. Hunter, E. Benavides, D. Samuelson, and M. Scheske, *Effective dose of dental CBCT—a meta analysis of published data and additional data for nine CBCT units.* Dentomaxillofacial Radiology, 2015. **44**(1): p. 20140197.
20. Stratis, A., G. Zhang, R. Jacobs, R. Bogaerts, and H. Bosmans, *Rotating and translating anthropomorphic head voxel models to establish an horizontal Frankfort plane for dental CBCT Monte Carlo simulations: a dose comparison study.* Physics in Medicine & Biology, 2016. **61**(24): p. N681.
21. Lee, C., J. Yoon, S.-S. Han, J.Y. Na, J.-H. Lee, Y.H. Kim, and J.J. Hwang, *Dose assessment in dental cone-beam computed tomography: Comparison of optically stimulated luminescence dosimetry with Monte Carlo method.* PloS one, 2020. **15**(3): p. e0219103.
22. Hartshorne, J., *Essential guidelines for using cone beam computed tomography (CBCT) in implant dentistry. Part 3: Radiation dose, risks, safety, ethical, and medico-legal considerations.* International Dentistry–African edition, 2018. **8**(5): p. 26-34.
23. Bolch, W.E., K. Eckerman, A. Endo, J.G.S. Hunt, D.W. Jokisch, C.H. Kim, K.P. Kim, C. Lee, J. Li, N. Petoussi-Henss, T. Sato, H. Schlattl, Y.S. Yeom, and M. Zankl, *ICRP Publication 143: Paediatric Reference Computational Phantoms.* Annals of the ICRP, 2020. **49**(1): p. 5-297.
24. Bolch, W., K. Eckerman, A. Endo, J. Hunt, D. Jokisch, C. Kim, K. Kim, C. Lee, J. Li, and N. Petoussi-Henss, *ICRP Publication 143: paediatric reference computational phantoms.* Annals of the ICRP, 2020. **49**(1): p. 5-297.
25. Adult, I., *Reference computational phantoms. ICRP publication 110.* Ann ICRP, 2009. **39**.
26. ICRP143. *paediatric computational reference phantoms*. 2020 [cited 2022 10/03]; Available from: https://www.icrp.org/publication.asp?id=ICRP%20Publication%20143.
27. Nolf, E., T. Voet, F. Jacobs, R. Dierckx, and I. Lemahieu, *An open-source medical image conversion toolkit.* Eur J Nucl Med, 2003. **30**(Suppl 2): p. S246.
28. Pieper, S., M. Halle, and R. Kikinis. *3D Slicer*. in *2004 2nd IEEE international symposium on biomedical imaging: nano to macro (IEEE Cat No. 04EX821)*. 2004. IEEE.
29. Valentin, J., *Basic anatomical and physiological data for use in radiological protection: reference values: ICRP*

Publication 89. Annals of the ICRP, 2002. **32**(3-4): p. 1-277.
30. Survey, N.H.a.N.E. 1988-1994 [cited 2024; Available from: https://wwwn.cdc.gov/nchs/nhanes/nhanes3/Default.aspx.
31. **(NIST), N.I.o.S.a.T.** [cited 2024; Available from: http://www.itl.nist.gov/div894/ovrt/projects/anthrokids.
32. Zajac, D.J. and L.D. Vallino, *Evaluation and management of cleft lip and palate: A developmental perspective*. 2016: Plural Publishing.
33. Berkowitz, S., *Cleft lip and palate*. 2006: Springer.
34. Rossell-Perry, P., *Atlas of Operative Techniques in Primary Cleft Lip and Palate Repair. 2020.* Switzerland: Springer.
35. Poludniowski, G., A. Omar, R. Bujila, and P. Andreo, *SpekPy v2. 0—a software toolkit for modeling x-ray tube spectra.* Medical Physics, 2021. **48**(7): p. 3630-3637.
36. Mohammed Ali, A., P. Hogg, M. Abuzaid, and A. England, *Impact of acquisition parameters on dose and image quality optimisation in paediatric pelvis radiography—A phantom study.* European Journal of Radiology, 2019. **118**: p. 130-137.
37. Hirsch, E., U. Wolf, F. Heinicke, and M. Silva, *Dosimetry of the cone beam computed tomography Veraviewepocs 3D compared with the 3D Accuitomo in different fields of view.* Dentomaxillofacial Radiology, 2008. **37**(5): p. 268-273.
38. Fisher, D.R. and F.H. Fahey, *Appropriate Use of Effective Dose in Radiation Protection and Risk Assessment.* Health Phys, 2017. **113**(2): p. 102-109.
39. Valentin, J., *Radiation and your patient: A guide for medical practitioners: ICRP Supporting Guidance 2: Approved by ICRP Committee 3 in September 2001*. 2001, SAGE Publications Sage UK: London, England. p. 1-52.